RESEARCH ARTICLE

High-resolution imaging of the excised porcine heart at a whole-body 7 T MRI system using an 8Tx/16Rx pTx coil

Maxim Terekhov[1] · Ibrahim A. Elabyad[1] · David Lohr[1] · Ulrich Hofmann[2] · Laura M. Schreiber[1]

Abstract

Introduction MRI of excised hearts at ultra-high field strengths ($B_0 \geq 7$ T) can provide high-resolution, high-fidelity ground truth data for biomedical studies, imaging science, and artificial intelligence. In this study, we demonstrate the capabilities of a custom-built, multiple-element transceiver array customized for high-resolution imaging of excised hearts.

Method A dedicated 16-element transceiver loop array was implemented for operation in parallel transmit (pTx) mode (8Tx/16Rx) of a clinical whole-body 7 T MRI system. The initial adjustment of the array was performed using full-wave 3D-electromagnetic simulation with subsequent final fine-tuning on the bench.

Results We report the results of testing the implemented array in tissue-mimicking liquid phantoms and excised porcine hearts. The array demonstrated high efficiency of parallel transmits characteristics enabling efficient pTX-based B_1^+-shimming.

Conclusion The receive sensitivity and parallel imaging capability of the dedicated coil were superior to that of a commercial 1Tx/32Rx head coil in both SNR and T_2^*-mapping. The array was successfully tested to acquire ultra-high-resolution ($0.1 \times 0.1 \times 0.8$ mm voxel) images of post-infarction scar tissue. High-resolution (isotropic 1.6 mm^3 voxel) diffusion tensor imaging-based tractography provided high-resolution information about normal myocardial fiber orientation.

Keywords Parallel transmit · RF-array · Excised heart · Ultra-high-field

Introduction

Ultra-high-field (UHF) ($B_0 \geq 7$ T) MRI systems provide significant improvements in signal-to-noise ratio (SNR) compared to clinical systems at lower field strengths (e.g., $B_0 \leq 3$ T). The effective RF wavelength in biological tissues at 7 T ($\lambda_{\text{eff}} \approx 12$ cm) approaches dimensions of the human anatomy (e.g., head or thorax), which results in constructive and destructive interference patterns, and hence transmit B_1 field (B_1^+) inhomogeneity [1, 2]. This problem can be addressed

using a parallel transmit (pTx) RF amplifier system in combination with an optimized multi-channel coil array. Shaping of a uniform B_1^+ field distribution within a region-of-interest (ROI) enabled by manipulation of magnitudes and phases of driving voltages of each Tx channel and performed in a static [3–10] or dynamic manner [11, 12] is known as "B_1^+-" or "RF-shimming". Multi-channel Tx arrays, driven by the pTx system, have enabled applications in target regions, for example, the human head [1, 13], prostate [9], heart [11, 12, 14–21], and torso [22, 23]. A wide variety of different coil array designs, e.g., strip line elements [24, 25], local Tx/Rx loop arrays [26–31], or dipole antennas [17, 32–35], allowed for significant progress in body imaging at UHF.

In recent studies, the feasibility of cardiac MRI (cMRI) in pigs at a 7 T scanner using different dedicated 16-element transceiver coil arrays was proven [36, 37]. Furthermore, significant advancements in both B_1^+-shimming and parallel imaging capabilities were demonstrated for *in-vivo* cMRI in pigs using an antisymmetric transceiver 8Tx/16Rx loop array with L-shaped elements [38]. The same concept was successfully implemented in the design of 7 T human

Maxim Terekhov and Ibrahim A. Elabyad have equally contributed to this work.

✉ Maxim Terekhov
Terekhov_M@ukw.de

1 Comprehensive Heart Failure Center (CHFC), Department of Cardiovascular Imaging, University Hospital Würzburg, Am Schwarzenberg 15, 97078 Würzburg, Germany

2 Department of Internal Medicine I / Cardiology, University Hospital Würzburg, Oberdürrbacher Straße 6, 97080 Würzburg, Germany

cardiac arrays [39]. Developed array designs enabled excellent parallel imaging characteristics with the capability of using high acceleration factors (up to $R = 6$) in 7 T cMRI. Finally, preliminary in-vivo results of the using antisymmetric concept of L-shaped elements for the high-density 8Tx/16Rx dipole array were reported [40].

MRI measurements of hearts *ex-vivo* at UHF can provide high-resolution ground truth data that complement *in-vivo* cMRI with image quality not compromised by physiologic motion. Moreover, scan times can be significantly longer than in animals or humans *in-vivo*. In extreme cases, scanning can be performed over many hours and, thus, can generate high-fidelity data for the assessment of morphological tissue properties like microstructure or tissue susceptibility effects [41–43]. For the highest SNR and spatial resolution, optimal transmit-and-receive characteristics are crucial factors. Available commercial coils for 7 T are usually designed for application in a specific body part (head, extremities) and may not always have optimal parameters for excised inner organs. In this study, we implemented a prototype of an 8Tx/16Rx transceiver array with antisymmetric L-shaped loop elements arranged on elliptically shaped housing and aimed to optimize a filling factor for an ultra-high-resolution 7 T MR-imaging of excised organs using a clinical whole-body scanner. The main goals were to validate the capabilities of the implemented array for (i) an efficient static parallel transmit B_1^+-shimming and (ii) parallel receive with high acceleration factors. The imaging performance of the new array was assessed, and pilot applications of high- and ultra-high spatial resolutions (up to 0.1 mm/pixel in-plane) multiparametric MR images were performed using excised porcine hearts.

Methods

The array is designed as a printed circuit board (PCB) with 16 loop elements bent around an elliptically shaped housing with major/minor axes of 12.3/10.7 cm (Fig. 1a,b). The elements were etched using 0.3 mm Cu trace of 4 mm width printed on a 0.3 mm FR4 substrate ($\varepsilon_r = 4.24$ and $\tan\delta = 0.014$ at 297.2 MHz). PCB was manufactured by Q-print Electronic GmbH (Heddesheim, Germany). The array was split into two sections to keep 5.4 cm spacing on the housing for routing the RF cables (Fig. 1c). The top and bottom sections comprised 10 and 6 elements, respectively, as shown in Fig. 1a. The dimensions of elements 1, 2, 7, 9, 11, 12 = 2.3×5.8 cm^2, elements 3, 4, 13, 14 = 3.5×3.5 cm^2, and elements 5, 6, 15, 16 = 2.2×6.9 cm^2. The decoupling between the central elements (1&2) and (11&12) was accomplished using a common conductor and shared decoupling capacitors (SDC) (C_1^d). The elements (3,4,5,6) and (13,14,15,16) were distributed in an antisymmetric manner

around the central loops of the top and bottom array sections, respectively. Elements 3 and 4 were decoupled with elements 1 and 2 using SDC (C_2^d). Elements 5, 7, and 9, and the identical elements 6, 8, and 10 were decoupled from the neighboring elements using capacitive decoupling (C_5^d, C_6^d, C_7^d, C_8^d, and C_9^d) using a decoupling gap of 9 mm. The total external dimensions for the top and bottom PCB parts were 18.9×12.8 cm^2 and 18.9×10.9 cm^2, respectively. To form an 8Tx/16Rx array compatible with the MRI system's 8 TX-channel RF Power Amplifier (RFPA), every two neighboring elements were combined in one Tx channel (Fig. 1c). The array was connected to a 16-channel interface with 16-Tx/Rx switches and 16-preamplifiers via four ODU plugs (ODU GmbH & Co. KG, Muehldorf, Germany). To adjust the default hardware-implemented phase shifts between the 16 coil elements, a discrete low-pass π-network phase shifter (PS) consisting of two equal capacitors and one non-magnetic inductor (Coilcraft, Inc., Silver Lake Road, Cary, IL, USA) was designed. These phase shifters were inserted between the coil elements feeding ports and the cable traps (CT) as shown in Fig. 1c.

A. EMF Simulations

EMF simulations were carried out using CST-MICRO-WAVE-STUDIO (CST-MWS, Dassault Systèmes SE, France) time-domain solver (transient solver), which is based on the finite integration technique (FIT). The CST mesh parameters were: 70 lines per wavelength, a lower mesh limit of 70, and a mesh line ratio limit of 80. A local mesh setting with an isotropic step width of 1 mm and an edge refinement factor of 4 was set for the curved Cu layouts. Open (add space) boundary condition was used. RF-circuit co-simulation [44] was employed in CST-Design-Studio (CST-DS) for matching and tuning to obtain an initial guess for the optimal lumped elements.

B. Interfacing of the array to a pTx RFPA

To interface the designed array to 8 Tx channels of RFPA, a pairing of elements was performed based on previous experience of designing arrays for pig and human MRI with L-shaped antisymmetricaly arranged elements [36, 37, 45]. For example, the elements (2&3) form an L-shaped pair connected to the RFPA-channel TX_0 (Fig. 1a, c). The same principle was used for the channels TX_2, TX_5, and TX_7. For the other elements, pairing the proximity between the nearest elements, and the shortest path to route the RF cables to the interface were taken into account. The complete pairing list is shown in Fig. 1c. The array was connected to the 8Tx/16Rx interface with 16-Tx/Rx switches and
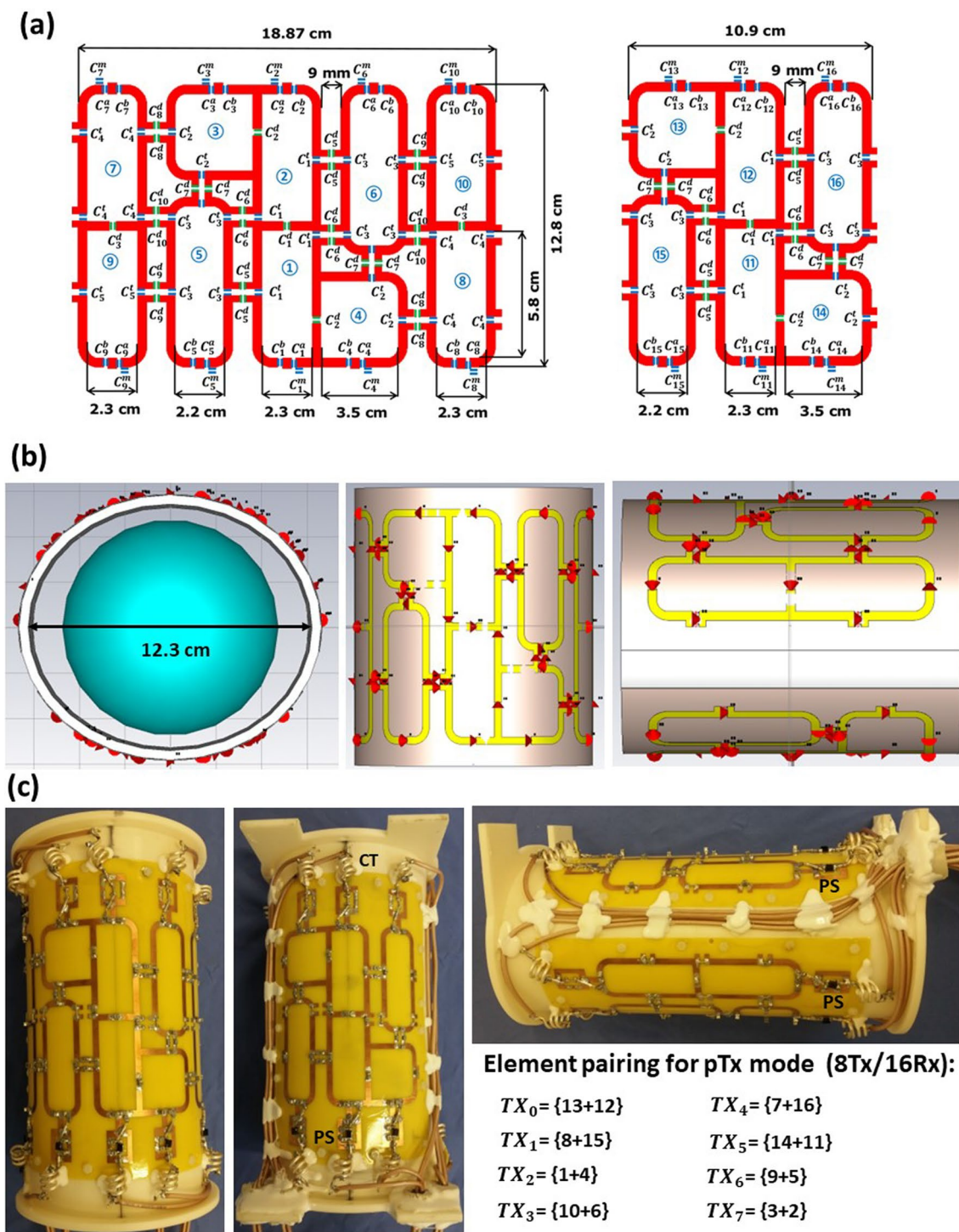
Fig. 1 Design and schematic of the ex-vivo array for high-resolution imaging of excised porcine hearts. **a** Coil elements layout, dimensions, and element numbering. **b** RF simulation model of the array loaded with a 10-cm spherical phantom in front, top, and side views. **c** A prototype of the 16-element antisymmetric array in the top, bottom, and side views. Phase shifters (PS) and cable traps (CT) are labeled accordingly. Every two neighboring loops are paired to be interfaced to the corresponding Tx channel of RFPA (channel numbering is according to the MRI system notation) to form an 8Tx/16Rx array configuration
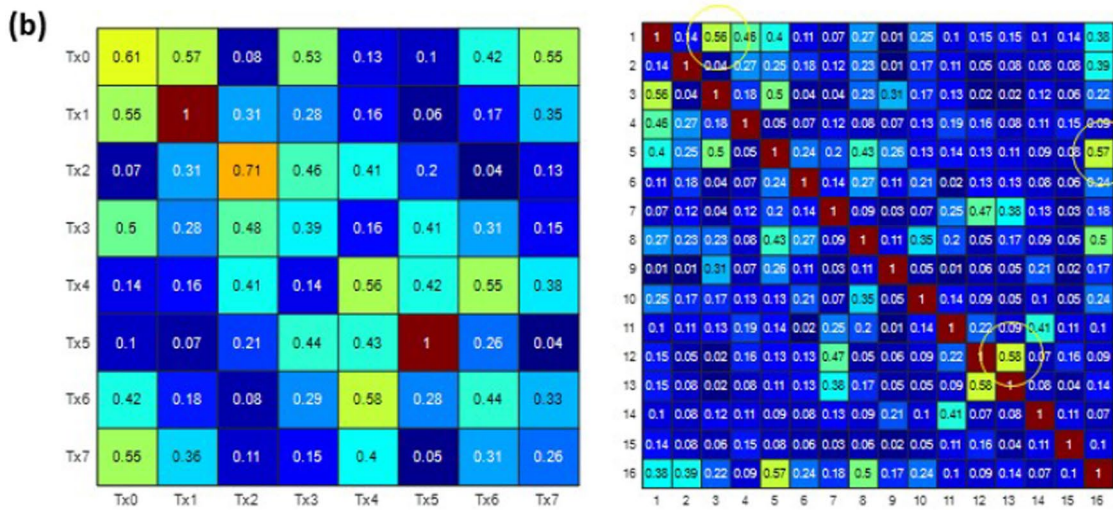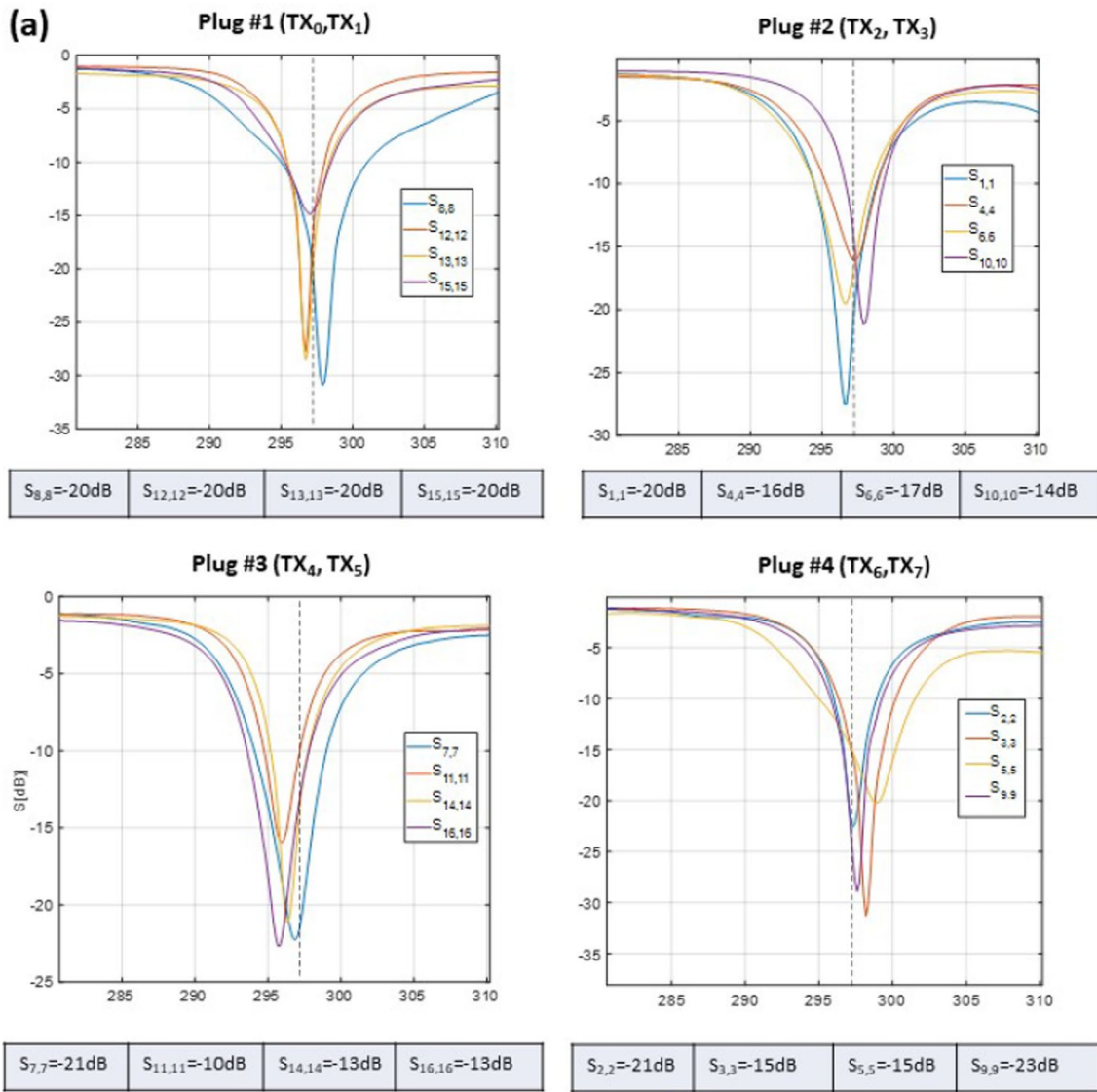
(a)

Plug #1 (TX0, TX1)

$S_{8,8}$=-20dB	$S_{12,12}$=-20dB	$S_{13,13}$=-20dB	$S_{15,15}$=-20dB

Plug #2 (TX2, TX3)

$S_{1,1}$=-20dB	$S_{4,4}$=-16dB	$S_{6,6}$=-17dB	$S_{10,10}$=-14dB

Plug #3 (TX4, TX5)

$S_{7,7}$=-21dB	$S_{11,11}$=-10dB	$S_{14,14}$=-13dB	$S_{16,16}$=-13dB

Plug #4 (TX6, TX7)

$S_{2,2}$=-21dB	$S_{3,3}$=-15dB	$S_{5,5}$=-15dB	$S_{9,9}$=-23dB

(b)

◄**Fig. 2 a** Measured S-parameters versus frequency for the four ODU plugs when the array was loaded with a 10-cm spherical phantom (ε_r=59.3 and σ=0.79 S/m). Most of the elements were matched better than -14 dB. Only elements 11 and 16 were matched to -10 and -13 dB. **b** The noise correlation coefficient matrix for 16 receive elements and normalized scattering matrix for 8 Tx channels measured by the MR scanner. Yellow circles on the noise correlation matrix show pairs with relatively high transmission coefficients (> -9 dB) leading to increased noise correlation

16-preamplifiers (Rapid Biomedical GmbH, Rimpar, Germany) via four plugs (ODU GmbH & Co. KG, Mühldorf a. Inn, Germany). The detailed scheme of interfacing can be found in supplementary materials of the work [40]. Each RFPA channel provides up to 2 kW peak power at the input interface plugs. The length of the feeding cables (between cable traps and interface sockets) is ~ 45 cm for one pair of plugs and ~ 25 cm for another pair.

C. Customer pTx-based B_1^+ shimming

The customer B_1^+ shimming procedure was implemented based on the so-called "relative" B_1-maps. These maps were reconstructed from complex GRE images acquired by driving individually each Tx-channel of the array and acquiring signal received simultaneously by all elements. It was demonstrated that such B_1^+ maps can be efficiently employed as a proxy of the absolute (flip-angle) B_1^+ maps to perform B_1^+ shimming in UHF MRI. A detailed description of the acquisition and reconstruction of relative B_1^+-maps used in both static and dynamic pTX-shimming procedures can be found in [11, 15, 46]. A brief mathematical description of the optimization problem and two cost functions used to promote the "B_1^+ homogeneity" and "B_1^+-efficiency", respectively, are provided in Appendix 1. The optimization was performed within the manually defined 3D volumes. For the homogeneous spherical phantom, the optimization volume was a cylinder with ~ 75 mm diameter and 50 mm height (as shown in Fig. 3). For the B_1^+-shimming in the excised heart sample, the optimization region was a rectangular slab with dimensions 60×60 x 60mm positioned to cover mid-myocardium and apical areas. The computed complex components of the array driving voltages for the individual Tx channels were set to the RFPA using B_1^+ adjustment platform of the MR scanner. To ensure a fair comparison between different pTX-shimming settings regarding transmit efficiency, the complex vectors of transmit voltages were normalized to have the unity norm (Appendix 1).

D. Sample preparation

Following the "3R" principle for testing the new array performance, we have used the excised hearts kindly provided after the authorized use of animals in other studies. The $n=3$

intact hearts of healthy piglets were obtained from project 55.2 2532–2-256 (District of Low Franconia, Germany). The heart of ~ 80 kg pig euthanized approximately 60 days after myocardial infarction, which was obtained from the study 55.2 DMS 2532–1134-16 (District of Low Franconia, Germany). The infarction was induced by 90 min balloon catheter occlusion of the left anterior descending coronary artery, followed by reperfusion. For the healthy pigs' hearts following the excision, the atria of the hearts was removed to ease the release of trapped air. Fixation was achieved via immersion in 10% neutral buffered formalin within 3 h of cardiac arrest. Hearts were placed in a plastic container and the sample position was fixed using sponges. The container was then slowly filled with Fomblin™ oil and excess air was removed from the sponges and the heart using a vacuum desiccator. Additionally, for B_1^+-shimming and coil characterization measurements, the homogeneous phantom was used. The phantom was implemented using a 100 mm diameter acryl glass sphere filled with the polyvinylpyrrolidone (PVP) water solution mimicking the electric properties of biological tissue [38].

E. MRI measurements

All measurements were performed using a whole-body 7 T MRI system (Magnetom™ "Terra") with 8-channel parallel transmit (pTx) system, (Siemens Healthineers, Erlangen, Germany). The characterization of receiving sensitivity and parallel imaging capabilities of the new array was done by comparison with the commercial 1Tx/32Rx head coil (Nova Medical, USA).

Array characterization for parallel receiving was performed using a dedicated vendor-supplied protocol (named "coil utility" on the Siemens MRI system). This protocol provides data acquisition using a fast spoiled GRE pulse sequence and reconstruction of SNR maps, g-factor maps, and noise correlation matrices. Imaging parameters were TR/TE = 9/3.8 ms, FA = 10^0, voxel size = 0.4×0.4x5mm, and matrix = 256×256. Measurements were performed in the described above homogenous spherical phantom and excised porcine hearts ($n=3$). To characterize and compare the receive sensitivity of the head coil and designed ex-vivo array, we used SNR maps reconstructed by the above-mentioned protocol. The SNR maps normalized using absolute B_1^+ maps are further referred to as receive sensitivity (RxS).

The absolute B_1^+ maps were acquired and reconstructed using the vendor-provided sequence "tfl_rfmap" based on the saturation-prepared turbo-FLASH pulse sequence [47]. For the off-line B_1^+ optimization, the relative B_1+ maps were acquired and reconstructed using the customized GRE sequence as described in works [9, 14, 15]. For both absolute and relative B_1^+ mapping, a fixed reference transmitter voltage $V_{ref}=100$ V was set via the scanner adjustment platform.

Customer B$_1^+$ static pTX-shimming in spherical phantom

(a) Normalized relative B$_1^+$ of individual Tx-channels (central slices)
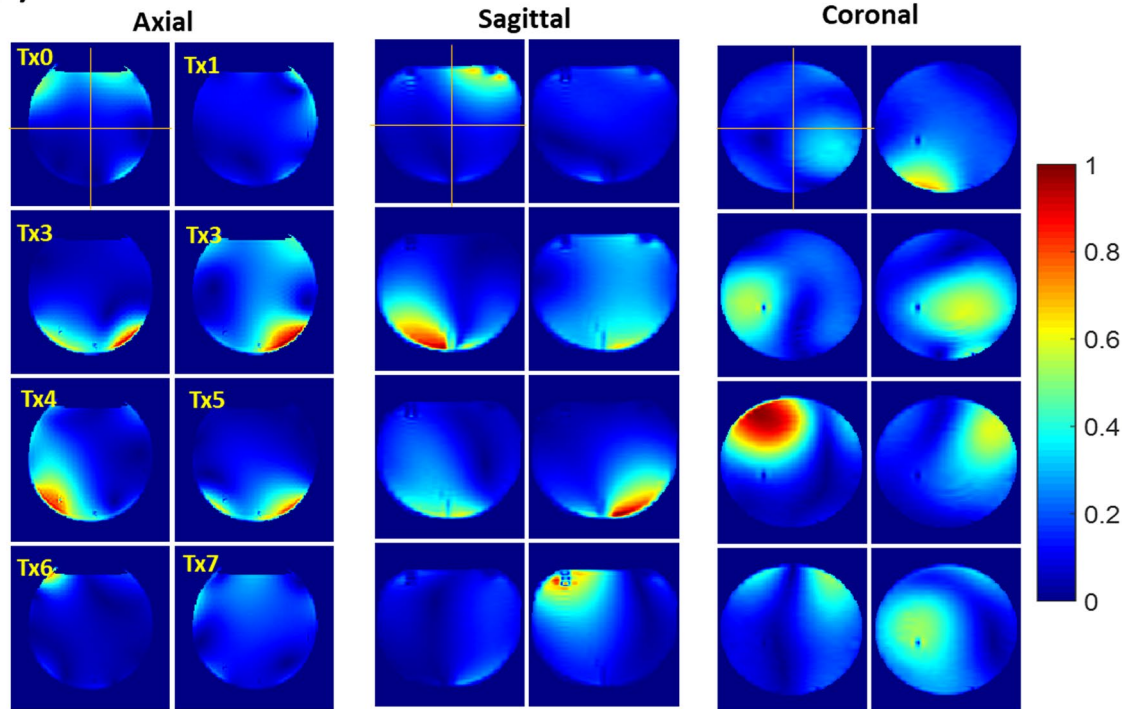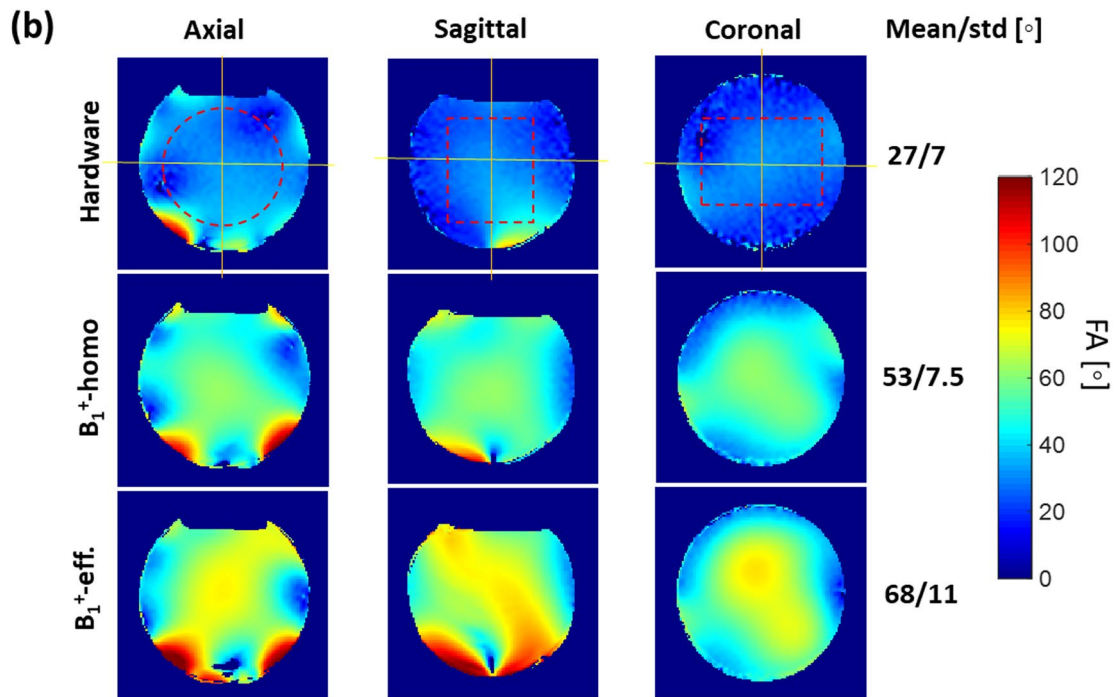

Combined absolute B$_1^+$

◄**Fig. 3** Static pTX-based B1+shimming in the homogeneous spherical phantom based on the customer optimization procedure (Appendix 1). (**a**) Relative normalized B1+maps of the individual channels used for B1+optimization. Central slice projections (solid lines) are shown. (**b**) Combined absolute B1+maps acquired with default array phasing ("Hardware") and using pTX-based RF-shimming settings computed within the labeled ROI (dashed red lines) by optimization of "B1+homogeneity" and "B1+efficiency" cost functions (Appendix 1). All three combined B1+maps are acquired with the same transmitter reference voltage of 100 V. The mean and standard deviation of the flip angle within shimming ROI are shown for each shimming setting

To visualize the effect of B_1^+-shimming in the volume, 3D GRE images of the spherical phantom were acquired with TE/TR = 3.2/20 ms, FA = 10^0, and voxel size = $1 \times 1 \times 2$ mm.

T_2^* maps with 1 mm isotropic resolution were generated from 2D gradient multi-echo sequence (mGRE) data acquired with both coils for the same heart sample.

Measurement parameters were: number of averages NA = 32, TR = 800 ms, 9 echoes per excitation with TE = [2.5.0.18.7] ms. To compare the parallel imaging capabilities of both coils, the mGRE data were acquired using consequently increasing the GRAPPA acceleration factor R = [2.0.6].

To assess the performance of the coil in ultra-high-resolution imaging of myocardial scar tissue after infarction, imaging was performed using a turbo-spin-echo sequence with the following parameters: echo train length = 4, TE/TR = 15/2000 ms, acquisition matrix = 960×810, slice thickness = 1.0 mm and 0.8 mm, physical pixel size in-plane = 0.1×0.1 mm, number of averages = 16, and acquisition time 42 min.

Diffusion tensor imaging (DTI) was performed using a spin echo diffusion sequence with Stejskal-Tanner diffusion encoding and EPI readout. To acquire a whole-heart DTI dataset with an isotropic spatial resolution of 1.6 mm, the vendor "epi_diff" pulse sequence was used with the

Fig. 4 Customer B1+shimming for the excised heart sample. (**a**) Normalized relative B1+-maps of the eight individual transmit channels (one axial slice shown). (**b**) Normalized combined relative B1-maps before pTx optimization (with hardware phases) and after pTx-based RF-shimming
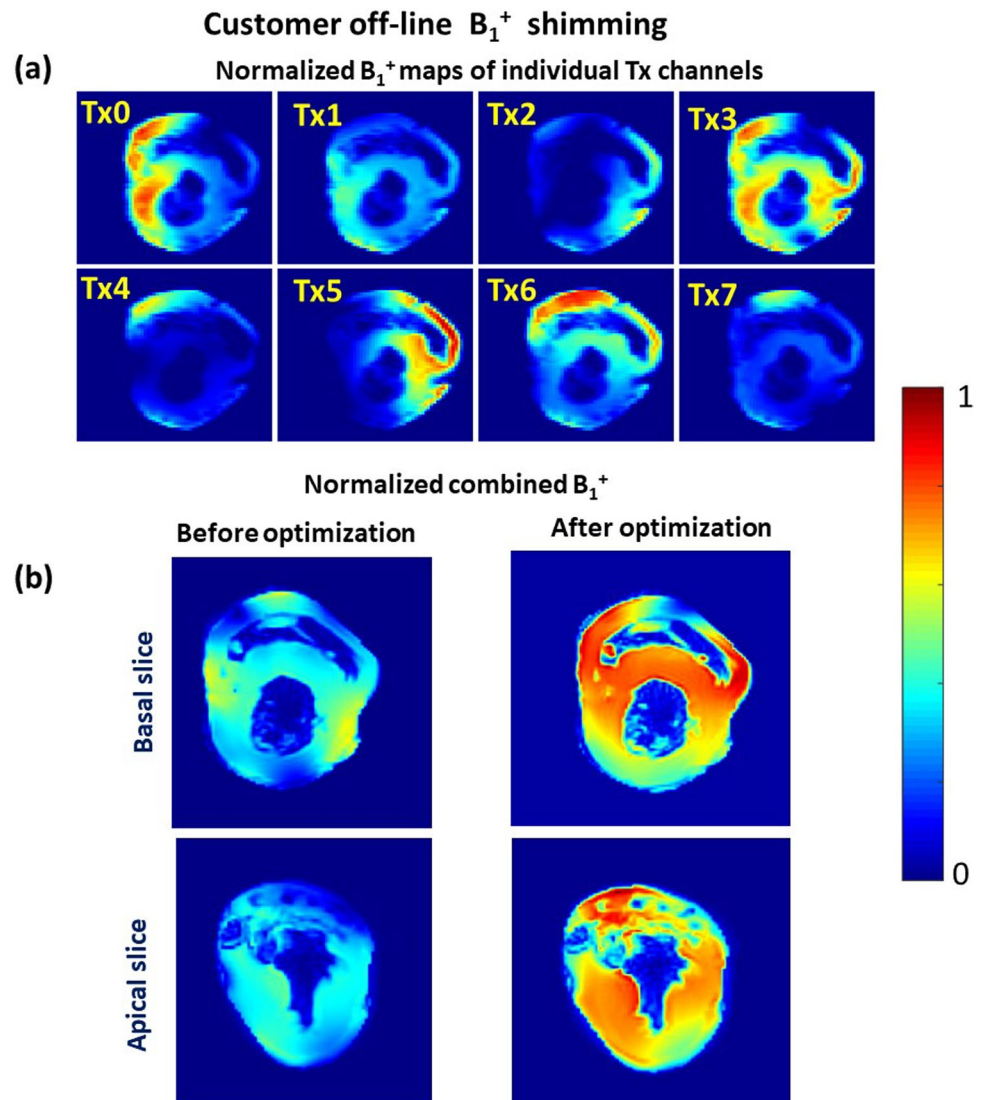
following parameters: TE $= 56$ ms, acceleration factor $R = 3$, 30 diffusion directions after Skare[48] (b $= 2000$s/ mm^2), frequency bandwidth $= 1414$ Hz/pixel, and 50 averages. DTI data processing and fiber-tracking reconstruction were done using DSI Studio[49] and Matlab (MathWorks, Natick, USA).

Results

Figure 2a shows measured S-parameter curves measured by VNA for the 16-element dedicated array versus frequency for the four ODU plugs when the array is loaded with a 10-cm spherical phantom filled with PVP solution (ε_r = 59.3 and $\sigma = 0.79$ S/m). Most of the elements were matched better than $- 14$ dB. Only elements 11 and 16 were matched to $- 10$ and $- 13$ dB. All 16 scattering curves demonstrate clean frequency profiles without splitting which would be evidence of insufficient element's decoupling. Figure 2b (left) shows S-matrix for 8 Tx channels measured by the scanner directional coupler (DICO) and saved by the RF-safety watchdog system. Figure 2b (right) demonstrates the noise correlation coefficient matrix. A high noise correlation

(> 0.5) is observed for 3 pairs of elements which are related to the high transmission coefficients (e.g., $S_{12,13} = - 8$ dB as measured by VNA). The increased transmission coefficient as well as uneven reflection coefficients in the 8-Tx S-matrix measured by the scanner DICO may be related to the inhomogeneous loading of the coil elements by the 10 cm spherical phantom.

Figure 3a demonstrates three central slices from the 3D relative B_1^+ maps acquired in the spherical phantom. These maps were used for the validation of the pTX-based B_1^+-shimming capability of the array. One can observe that the localizations of the regions with maximal intensity in the B_1^+ profiles of the individual Tx channels are well separated which is a prerequisite for an efficient static B_1^+-shimming. Absolute B_1^+ maps for the same slices are shown in the Supplementary Materials (Figure S1). Panel 3b shows absolute combined B_1^+-maps before and after RF-shimming performed using cost functions optimizing B_1^+-homogeneity and B_1^+-efficiency represented, respectively, by Eq. (2) and Eq. (3) of Appendix 1. The optimization using the former cost function improved the coefficient-of-variation of the flip-angle within the optimized volume by about factor 2, whereas using the latter cost function increased the mean
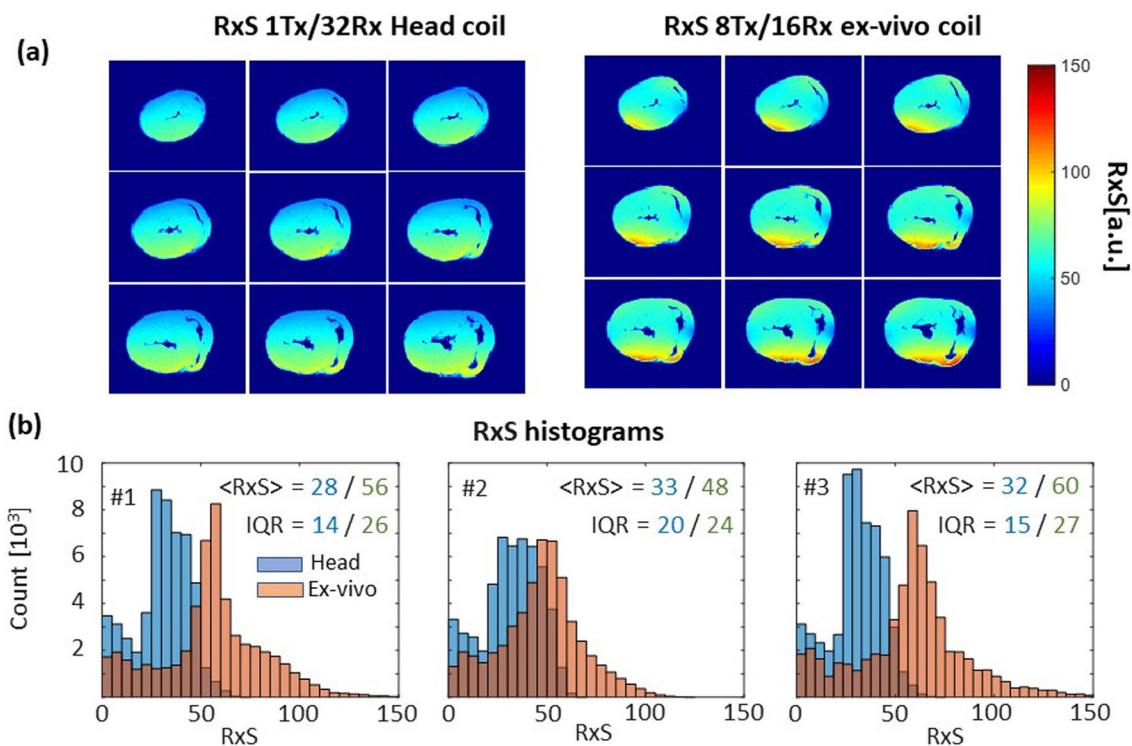

Fig. 5 Rx-sensitivity comparison for head coil and ex-vivo coil. (**a**) Example of Rx-sensitivity maps (9 slices of 32) acquired using ex-vivo array in the heart sample #3 in comparison to the same slices acquired with 1Tx/32Rx head coil. A higher mean value of normalized SNR is observed visually for the ex-vivo array. **b** Histograms of Rx-sensitivity for 3 ex-vivo heart samples for the head coil (blue bars) and ex-vivo array (red bars). The advantage of the ex-vivo array in filling factor manifests in essentially higher mean Rx-sensitivity. The larger heterogeneity (characterized by interquartile range) of normalized SNR is, however, a consequence of smaller Tx/Rx ex-vivo array volume compared to the resonator of the head coil

flip-angle value by 150%. Supplementary material Figure S2 shows the effect of using the computed optimized B_1^+-shimming settings on the acquired GRE images. Using the same RF-pulse voltages, the signal intensities within the optimization volume were increased by factor > 2 by applying both optimized RFPA voltages settings for the B_1^+ shimming.

Figure 4a,b shows the individual relative B_1^+ maps and the resulting combined B_1^+ field in the excised heart sample before and after the B_1^+ shimming targeted for the B_1^+-efficiency. Despite the size of the excised heart being relatively small compared to the spherical phantom, the peaks of B_1^+ profiles of most of the individual TX channels are well localized within the sample. Therefore, the optimization procedure is capable to increase significantly both homogeneity and the mean value of the combined B_1^+.

Figure 5a, b shows a comparison of Rx-sensitivity maps and histograms for both the 1Tx/32Rx head coil and the new 8Tx/16Rx array. Whereas homogeneity of the RxS (IQR metric) is higher for the head coil with a large volume resonator and essentially larger size of Rx array, we found that Rx-sensitivity is up to factor 2 times higher for the new ex-vivo array because of the optimal filling factor.

Figure 6a shows the g-factor maps of the 1Tx/32Rx head coil and the 8Tx/16Rx ex-vivo array in the mid-myocardium slice of the excised heart sample. Despite the difference by a factor of two in the number of receiving elements of both coils the statistical metrics of the g-factor (mean value and 98-percentile) are very similar at acceleration factors $R = 2,3$ and 4. For the higher acceleration factors ($R = 5$ and 6), these metrics are lower for the new ex-vivo array compared to the head coil.

Figure 6b shows a representative slice of the T_2^* maps in an excised heart acquired with both coils using GRAPPA parallel receive acceleration factors between 2 and 6. One can observe that at high acceleration factors $R = 4, 5,$ and 6, the T_2^* maps acquired with the head coil show more "salt-pepper"-like noise compared to the maps acquired with the new array. Accordingly, the heterogeneity of T_2^* values, characterized by the interquartile range, increases for the head coil more significantly (up to 20% at $R = 5$ and 6) than that for the new array.

Figure 7a, b shows ultra-high-resolution images of scar tissue in the excised heart. The images demonstrate a very high level of detail in both heart anatomy (a) and especially scar tissue structure within the myocardial wall. Sub-millimeter slice thickness allows for resolving the 3D network of the scar within the myocardial wall including the structure of scar edges (peri-infarct area). This transition zone between scar and intact tissue is especially important diagnostically for identifying the risk of malignant arrhythmias and sudden cardiac death [50].

Figure 8 shows representative high-resolution tractography visualizing distinct structures of myocardial fiber orientation in the intact heart. High isotropic spatial resolution enabled detailed visualization of papillary muscle (dark blue), the intersection of the left and right ventricle (panel b), and the helical configuration of myocyte bundles with a transmural variation of the helix angle (panel c). The further DTI results presenting fractional anisotropy, principal eigenvalues, and helix angle and E2A angle maps are shown in the Supplementary Materials (Figure S3).

Discussion

Due to a lack of commercially available coils for imaging excised tissue, most researchers typically use standard RF arrays designed for clinical applications in humans. We demonstrated the concept of the inexpensive dedicated array for UHF-MR-imaging of excised hearts based on 16 loop elements with an antisymmetric L-shaped arrangement used for both parallel transmit-and-receive. The unitary architecture based on the single printed PCB requires moderate hardware and manpower resources for implementation in comparison to the coils using separate transmit-and-receive parts. The comparison of the new excised tissue array with the conventional head coil provided remarkable insights. Despite the small dimensions of the dedicated array targeted to provide a high filling factor for an excised heart, a static pTX RF-shimming allowed for significant (by factor > 2) improvement of B_1^+ homogeneity and efficiency. This is an interesting finding in such a relatively small coil, because, typically, pTx techniques at 7 T are applied for B_1^+ shimming in relatively large objects. A higher filling factor of the new array provided a factor two increased Rx-sensitivity when compared with the 1Tx/32Rx channel head coil.

Results in parallel receive mode tended to be interesting. Despite two times fewer amount of receive elements, the g-factor of the new array was found to be superior to that of the head coil 32Rx-only array, especially for the high acceleration factor $R > 4$. This is probably an effect of optimal dimensions and geometry. Remarkably less "salt-pepper"-like noise GRAPPA reconstruction artifacts were observed in T_2^* maps reconstructed from images acquired with acceleration $R = 4.0.6$ using the new 8Tx/16Rx transceiver array in comparison to the commercial 1Tx/32Rx head coil with separated Tx-resonator and Rx array.
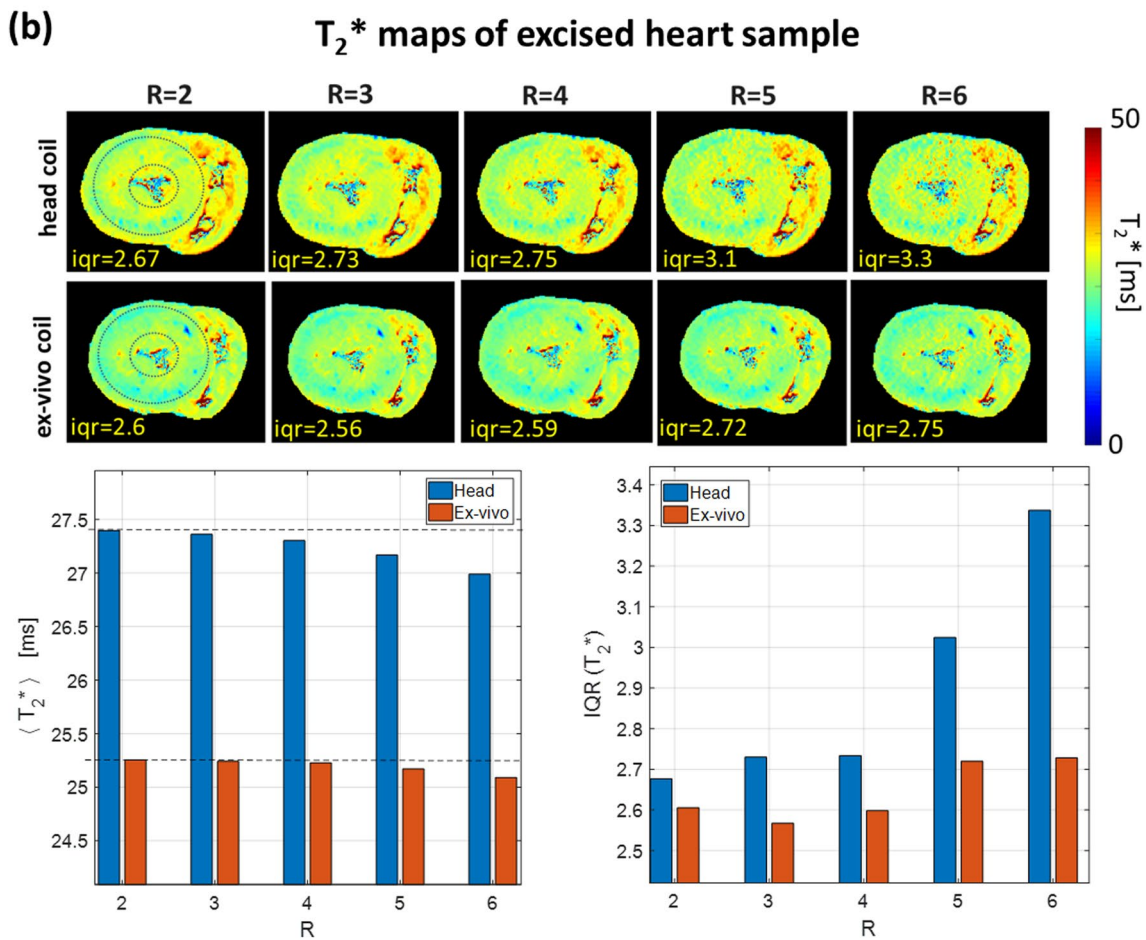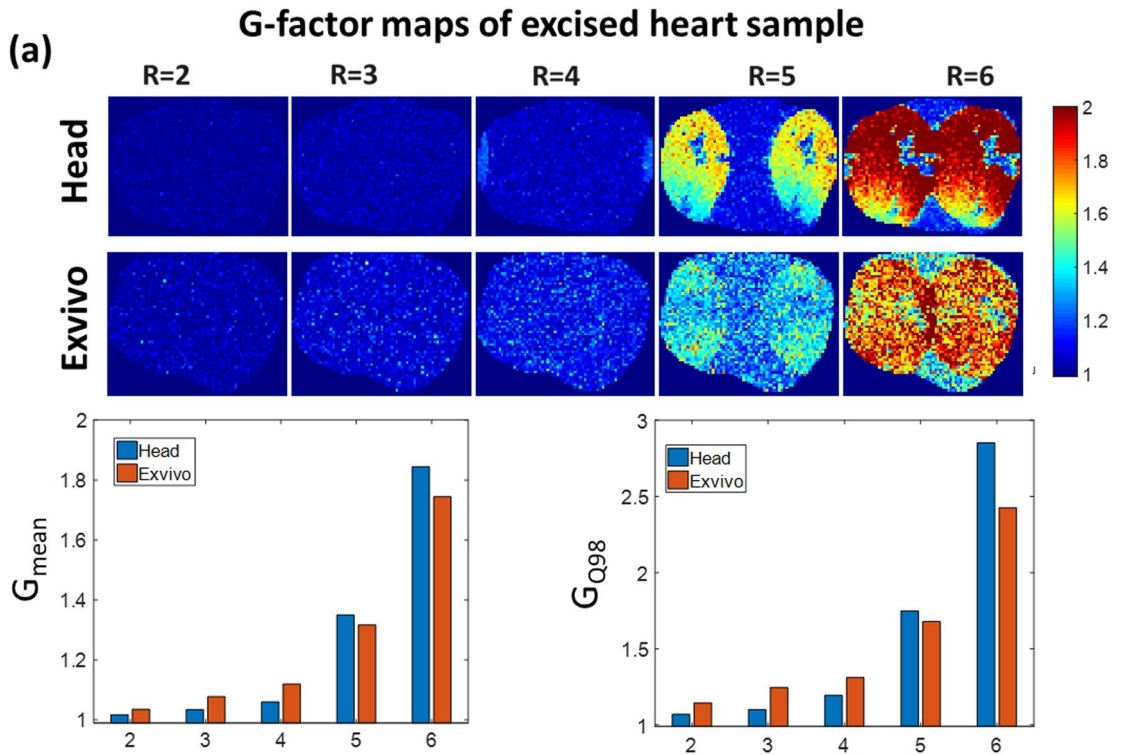
(a)

G-factor maps of excised heart sample

(b)

T$_2$* maps of excised heart sample

◄**Fig. 6** Noise amplification in parallel acquisition imaging. (**a**) Maps of the g-factor and statistical metrics for both coils measured in the excised heart sample #3. The mean and maximal (98-percentile) g-factor values become higher for the head coil for the high acceleration factors $R = 5,6$. **b** T2* maps of heart sample #3, reconstructed from mGRE images using increasing GRAPPA acceleration factors. There is a remarkable increase of the noise amplification at ($R = 5,6$) for the head coil leading to 20% increase T2* IQR values within the marked (dashed line) myocardial region when compared with results obtained with the new excised tissue coil

The coil demonstrated outstanding potential to perform post-mortem non-invasive "MRI-histology"-similar images of the heart both at sub-millimeter (100 μm) level using ultra-high-resolution multiparametric imaging (proton density, T_2, T_2^*) and on the microscopic level using diffusion-based MRI tractography of the cardiac muscles. Future applications in diffusion imaging will greatly benefit from the low noise amplification and a minimal level of reconstruction artifacts even at high parallel imaging acceleration. The latter is of high importance for DTI application at 7 T because of the possibility to reduce echo time in EPI readout and, thus, to minimize SNR losses due to short T_2^* at 7 T, in particular, in fixed hearts [41] or other specimens. The resulting high image resolution (≤ 1.6 mm isotropic) will enable the assessment of anatomical regions previously hardly accessible, e.g., the intersection of the left and right ventricle or the right ventricle [51]. Overall, ex-vivo imaging in general, and excised tissue imaging in particular, provide valuable supplementary information and enforce a close linkage between *in-vivo* MRI and optical microscopic data for histology. Moreover, such MRI data may become important as high-fidelity ground truth in the development of machine and deep learning applications, in situations where such data cannot be acquired in-vivo or where in-vivo acquisitions are not feasible because of patient or animal constraints.

Furthermore, the dedicated array for excised tissue imaging is helpful in studies on the validation of new MRI applications. Potentially, the dedicated coil for MRI of the excised heart can be used in large-animal adapted Langendorf-type models [52, 53] Another potential research field may be human hearts after excision due to cardiac transplantation or in xenotransplantation research. The mentioned beating hearts may also be studied by extension of the coil with a dedicated organ chamber and perfusion system. Further fields of in-vivo application may be preclinical imaging of middle-size small animals (e.g., guinea pigs, rats, and small rabbits) performed in the clinical scanner or human imaging of the wrist or elbow.

The drawback of the compact size of the new array is the proximity effect of relatively small loop elements leading to the signal inhomogeneity near the array surface and requiring additional efforts for the normalization of signal intensities. It puts additional demands on the fidelity of the MRI system's receive chain, which imposes no problem with today's scanners' receive systems' dynamic range, and with adequate adjustment of the receive chain for the object under investigation. Another limitation of the study was the use of the Fomblin™ environment for the allocation of the pig hearts used in this study. Fomblin™ has a low electric permittivity that leads to a less sophisticated standing wave pattern with the array volume. However, submersing tissue in the synthetic oil may lead to alterations in the biological properties of the tissue [41] and would not allow experiments with perfused hearts. As an alternative, fresh non-fixed excised hearts could be placed within an isotonic NaCl–water solution with high permittivity ($\varepsilon = 79$) which is essentially more challenging for the B_1^+-shimming. A second limitation was using only a static pTX B_1^+-shimming in all studies. Further improvement of SNR and its homogeneity may be achieved using dynamic pTX B_1^+-shimming with tailored [12] or universal pTX pulses [11].

Conclusion

We presented the novel concept of a dedicated array for ultra-high-resolution MRI of excised pig hearts on a clinical whole-body MRI system. The prominent features of the array are (i) the 8TX/16Rx architecture based on 16 antisymmetrically allocated loops for the parallel transmit-and-receive combined with (ii) the dimensions optimized for the small targeted sample volume. Up to factor 2 gain of receive sensitivity in comparison to the commercial 1 T/32Rx head coil was achieved in the pilot study. The capability to provide an efficient B_1^+ shimming based on the pTX platform and, at the same time, ensuring a robust parallel imaging capability for high- and ultra-high-resolution multiparametric MRI of excised pig hearts were demonstrated.

Appendix 1: Customer pTx-based static B_1^+-shimming

The combined B_1^+ field created by the transceiver array is expressed as

$$B_{1c}^+(r) = \left| \sum_{k=0}^{N} C_k s_k^+(r) \right|, \tag{1}$$

where, $C_k = |C_k| e^{i\varphi_k}$ are the complex weights of the driving current of channels and $s_k^+(r)$ are spatial B_1^+ maps of the individual array elements. Static pTx B_1^+ shimming is performed by manipulation of the transmit vector $\{C\} = \{C_1 \cdots C_N\}$.

Fig. 7 Ultra-high spatial resolution images of an excised heart 60 days after infarction. The top row shows a single slice with a whole-heart long-axis view and zoomed region of the scar (labeled by the yellow rectangle). The bottom row shows zoomed regions of individual slices covering the scar region. Images were acquired with parallel receive acceleration factors $R = 2$ (top row slice thickness 1 mm, acquisition time ~ 55 min) and $R = 3$ (bottom row, slice thickness 0.8 mm, acquisition time ~ 40 min), respectively. In both cases, a very high level of detail is observed in post-infarction scar tissue
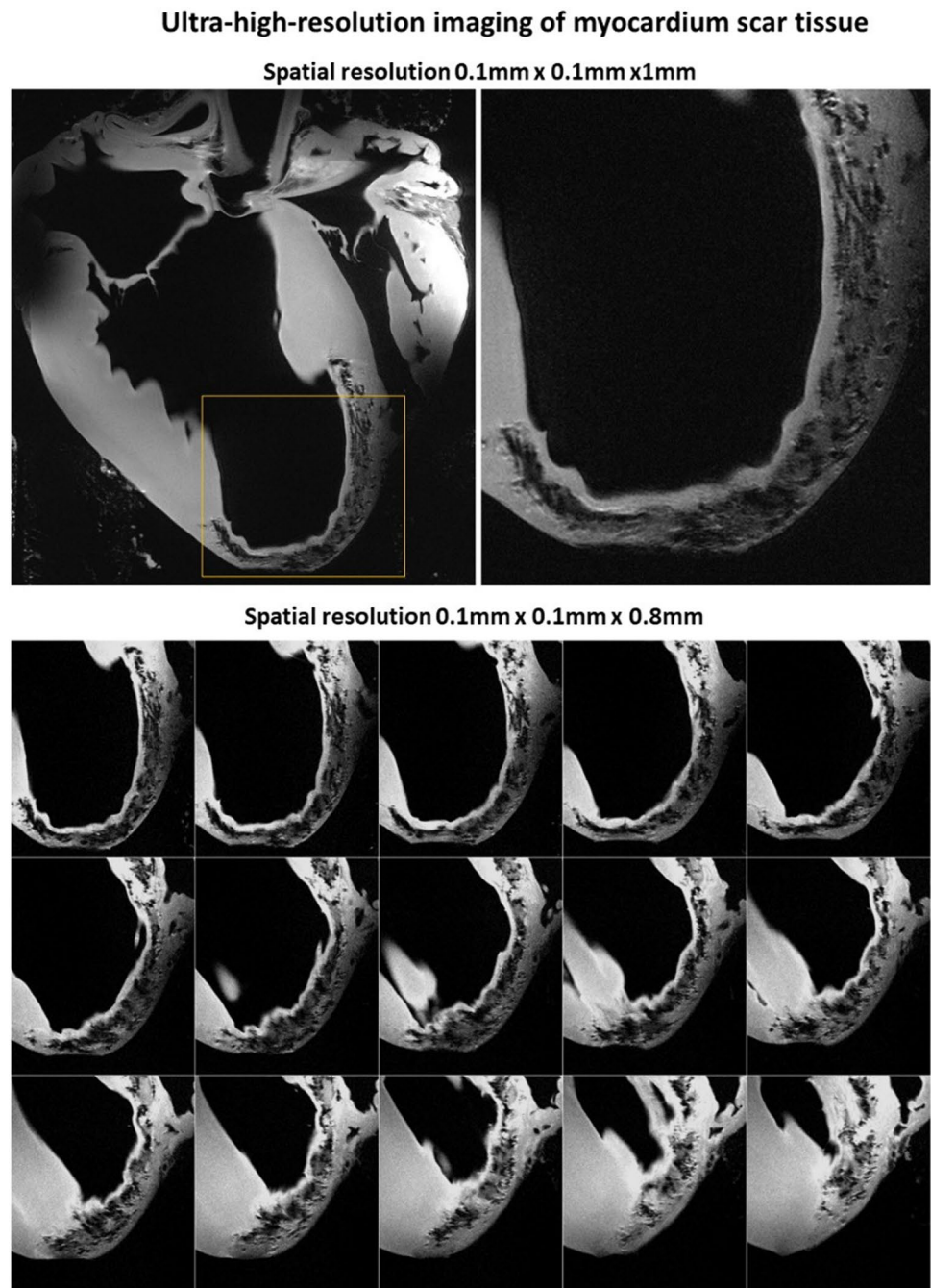
Two cost functions based on statistical metrics of $B_{1c}^+(r)$ computed within the volume Δr were defined as

$$F_{homo}(\Delta r, \{C\}) = \left(\frac{std\left(B_{1c}^+(r)\right)}{mean\left(B_{1c}^+(r)\right)} \right)\left(\frac{mean\left(B_{1c}^+(r)\right)}{max\left(B_{1c}^+(r)\right) - min\left(B_{1c}^+(r)\right)} \right)^{-1} \quad (2)$$

$$F_{eff}(\Delta r, \{C\}) = \left(\frac{std(B_{1c}^+(r))}{mean(B_{1c}^+(r))} \right)min\left(B_{1c}^+(r)\right)^{-1} \quad (3)$$

The first function is aimed to minimize the coefficient-of-variation and difference between maximal and minimal value and, thus, to promote the homogeneity of B_1^+

$$TX_e(\Delta r, \{C\}) = \frac{\left| \sum_k^N C_k s_k^+ \right|}{\sum_k^N \left| C_k s_k^+ \right|}. \tag{4}$$

Finally, the optimization problem is to be solved regarding the transmission vector

$$\{C_{opt}\} = argmin\left(\frac{F_{cost}(\Delta r, \{C\})}{TX_e(\Delta r, \{C\})} \right). \tag{5}$$

Problem (5) was solved by the multi-start application of a constrained minimization solver using the MATLAB optimization toolbox and an in-house developed toolbox for RF-shimming [54]. The normalization boundary conditions for the individual components of the vector $\left| C_k \right| \leq 1$ were used to ensure limited RFPA power in each channel. The found optimization vectors were normalized as $\| C_{opt} \| = 1$. The normalized complex vectors were set to the RFPA using the "patient-specific" mode of the B_1^+ adjustment of the scanner.

Declarations

Conflict of interest The authors declare that they have no conflicts of interest.

Ethical standards This paper does not contain any data of studies performed with human participants or living animals. Following the "3R"

Fig. 8 Tractography of myofiber bundles based on high-resolution DTI imaging of a fixed porcine heart acquired using the new coil. **a** Tractography showing 30,000 fiber bundle tracts visualized using tubes with a thickness of 5% of the voxel size. Thresholds for tracking were FA: 0.1, min bundle lengths: 10 mm, max bundle lengths: 300 mm, step size: 0.5 of the voxel size, and angle: 60°. Color-coding of the tracts corresponds to the main eigenvector orientation. A respective coordinate system is given in the bottom left. The dashed box approximates the position of the slab shown in (**b**) and (**c**). (**b**) Excerpt (thickness corresponds to three slices) from the whole-heart tractography. The high resolution enables the visualization and assessment of papillary muscle (dark blue) within the left and right ventricle or the transmural helical configuration of myocyte bundles as well as the intersection of the left and right ventricle with a fidelity unobtainable in-vivo. Color-coding of the tracts corresponds to the main eigenvector orientation as in (**a**). (**c**) The same tractography excerpt with color-coding of the tracts corresponds to the local helix angle value

distribution is referred as "B_1^+-homogeneity". The second function aimed for the suppression of destructive interferences via maximizing a minimum of B_1^+ within optimization volume is referred to as "B_1^+-efficiency".

Additionally, the cost function included the array transmit efficiency ratio of "sum-of-magnitudes" (SOM) and "magnitude-of-sum" (MOS) is defined as

principle the excised organs kindly provided after the authorized use of animals in other studies were used.

References

1. Van de Moortele PF, Akgun C, Adriany G, Moeller S, Ritter J, Collins CM, Smith MB, Vaughan JT, Ugurbil K (2005) B(1) destructive interferences and spatial phase patterns at 7 T with a head transceiver array coil. Magn Reson Med 54(6):1503–1518

2. Ibrahim TS, Lee R, Abduljalil AM, Baertlein BA, Robitaille PM (2001) Dielectric resonances and B(1) field inhomogeneity in UHFMRI: computational analysis and experimental findings. Magn Reson Imaging 19(2):219–226

3. Xin SX, Huang QH, Gao Y, Li BG, Xu YK, Chen WF (2013) Fetus MRI at 7 T: B-1 shimming strategy and SAR safety implications. IEEE Trans Microw Theory Tech 61(5):2146–2152

4. Ibrahim TS (2006) Ultrahigh-Field MRI whole-slice and localized RF field excitations using the same RF transmit array. IEEE Trans Med Imaging 25(10):1341–1347

5. Mao W, Smith MB, Collins CM (2006) Exploring the limits of RF shimming for high-field MRI of the human head. Magn Reson Med 56(4):918–922

6. Collins CM, Liu W, Swift BJ, Smith MB (2005) Combination of optimized transmit arrays and some receive array reconstruction methods can yield homogeneous images at very high frequencies. Magn Reson Med 54(6):1327–1332

7. Yoo H, Gopinath A, Vaughan JT (2012) A method to localize RF B-1 field in high-field magnetic resonance imaging systems. IEEE Trans Biomed Eng 59(12):3365–3371

8. Elabyad IA, Herrmann T, Bruns C, Bernarding J, Erni D (2018) RF shimming and improved SAR safety for MRI at 7 T with combined Eight-element stepped impedance resonators and traveling-wave antenna. IEEE Trans Microw Theory Tech 66(1):540–555

9. Metzger GJ, Snyder C, Akgun C, Vaughan T, Ugurbil K, Van de Moortele PF (2008) Local B1+ shimming for prostate imaging with transceiver arrays at 7T based on subject-dependent transmit phase measurements. Magn Reson Med 59(2):396–409

10. Adriany G, Van de Moortele PF, Wiesinger F, Moeller S, Strupp JP, Andersen P, Snyder C, Zhang X, Chen W, Pruessmann KP, Boesiger P, Vaughan T, Ugurbil K (2005) Transmit and receive transmission line arrays for 7 tesla parallel imaging. Magn Reson Med 53(2):434–445

11. Aigner CS, Dietrich S, Schaeffter T, Schmitter S (2022) Calibration-free pTx of the human heart at 7T via 3D universal pulses. Magn Reson Med 87(1):70–84

12. Schmitter S, DelaBarre L, Wu X, Greiser A, Wang D, Auerbach EJ, Vaughan JT, Ugurbil K, Van de Moortele PF (2013) Cardiac imaging at 7 Tesla: Single- and two-spoke radiofrequency pulse design with 16-channel parallel excitation. Magn Reson Med 70(5):1210–1219

13. Adriany G, Van de Moortele PF, Ritter J, Moeller S, Auerbach EJ, Akgun C, Snyder CJ, Vaughan T, Ugurbil K (2008) A geometrically adjustable 16-channel transmit/receive transmission line array for improved RF efficiency and parallel imaging performance at 7 Tesla. Magn Reson Med 59(3):590–597

14. Aigner CS, Dietrich S, Schmitter S (2021) Three-dimensional static and dynamic parallel transmission of the human heart at 7 T. Nmr in Biomedicine 34 (3).

15. Dietrich S, Aigner CS, Kolbitsch C, Mayer J, Ludwig J, Schmidt S, Schaeffter T, Schmitter S (2021) 3D Free-breathing multichannel absolute B-1(+) Mapping in the human body at 7T. Magn Reson Med 85(5):2552–2567

16. Schar M, Ding H, Herzka DA (2015) Improvement in B1+ homogeneity and average flip angle using dual-source parallel rf excitation for Cardiac MRI in swine hearts. PLoS ONE 10(10):e0139859

17. Steensma BR, Voogt IJ, Leiner T, Luijten PR, Habets J, Klomp DWJ, van den Berg CAT, Raaijmakers AJE (2018) An 8-channel Tx/Rx dipole array combined with 16 Rx loops for high-resolution functional cardiac imaging at 7 T. Magn Reson Mater Phys, Biol Med 31(1):7–18

18. Dietrich S, Aigner CS, Kolbitsch C, Mayer J, Ludwig J, Schmidt S, Schaeffter T, Schmitter S (2020) 3D Free-breathing multichannel absolute B1+Mapping in the human body at 7T. Magn Reson Med. https://doi.org/10.1002/mrm.28602

19. Niendorf T, Graessl A, Thalhammer C, Dieringer MA, Kraus O, Santoro D, Fuchs K, Hezel F, Waiczies S, Ittermann B, Winter L (2013) Progress and promises of human cardiac magnetic resonance at ultrahigh fields: a physics perspective. J Magn Reson 229:208–222

20. Niendorf T, Paul K, Oezerdem C, Graessl A, Klix S, Huelnhagen T, Hezel F, Rieger J, Waiczies H, Frahm J, Nagel AM, Oberacker E, Winter L (2016) W(h)ither human cardiac and body magnetic resonance at ultrahigh fields? technical advances, practical considerations, applications, and clinical opportunities. NMR Biomed 29(9):1173–1197

21. Niendorf T, Schulz-Menger J, Paul K, Huelnhagen T, Ferrari VA, Hodge R (2017) High Field Cardiac Magnetic Resonance Imaging: A Case for Ultrahigh Field Cardiac Magnetic Resonance. Circ Cardiovasc Imaging 10 (6).

22. Erturk MA, Raaijmakers AJ, Adriany G, Ugurbil K, Metzger GJ (2017) A 16-channel combined loop-dipole transceiver array for 7 tesla body MRI. Magn Reson Med 77(2):884–894

23. Wu X, Schmitter S, Auerbach EJ, Ugurbil K, Van de Moortele PF (2014) Mitigating transmit B 1 inhomogeneity in the liver at 7T using multi-spoke parallel transmit RF pulse design. Quant Imaging Med Surg 4(1):4–10

24. Vaughan JT, Snyder CJ, DelaBarre LJ, Bolan PJ, Tian J, Bolinger L, Adriany G, Andersen P, Strupp J, Ugurbil K (2009) Whole-body imaging at 7T: preliminary results. Magn Reson Med 61(1):244–248

25. Snyder CJ, DelaBarre L, Metzger GJ, van de Moortele PF, Akgun C, Ugurbil K, Vaughan JT (2009) Initial results of cardiac imaging at 7 Tesla. Magn Reson Med 61(3):517–524

26. Graessl A, Renz W, Hezel F, Dieringer MA, Winter L, Oezerdem C, Rieger J, Kellman P, Santoro D, Lindel TD, Frauenrath T, Pfeiffer H, Niendorf T (2014) Modular 32-channel transceiver coil array for cardiac MRI at 70T. Magn Reson Med 72(1):276–290

27. Dieringer MA, Renz W, Lindel T, Seifert F, Frauenrath T, von Knobelsdorff-Brenkenhoff F, Waiczies H, Hoffmann W, Rieger J, Pfeiffer H, Ittermann B, Schulz-Menger J, Niendorf T (2011) Design and application of a four-channel transmit/receive

surface coil for functional cardiac imaging at 7.T. J Magn Reson Imaging 33(3):736–741

28. Winter L, Kellman P, Renz W, Gräßl A, Hezel F, Thalhammer C, von Knobelsdorff-Brenkenhoff F, Tkachenko V, Schulz-Menger J, Niendorf T (2012) Comparison of three multichannel transmit/receive radiofrequency coil configurations for anatomic and functional cardiac MRI at 70.T: implications for clinical imaging. Eur Radiol 22(10):2211–2220

29. Grassl A, Winter L, Thalhammer C, Renz W, Kellman P, Martin C, von Knobelsdorff-Brenkenhoff F, Tkachenko V, Schulz-Menger J, Niendorf T (2013) Design, evaluation and application of an eight channel transmit/receive coil array for cardiac MRI at 7.0 T. Eur J Radiol 82(5):752–759

30. Thalhammer C, Renz W, Winter L, Hezel F, Rieger J, Pfeiffer H, Graessl A, Seifert F, Hoffmann W, von Knobelsdorff-Brenkenhoff F, Tkachenko V, Schulz-Menger J, Kellman P, Niendorf T (2012) Two-dimensional sixteen channel transmit/receive coil array for cardiac MRI at 7.0 T: design, evaluation, and application. J Magn Reson Imaging 36(4):847–857

31. Versluis MJ, Tsekos N, Smith NB, Webb AG (2009) Simple RF design for human functional and morphological cardiac imaging at 7tesla. J Magn Reson 200(1):161–166

32. Avdievich NI, Solomakha G, Ruhm L, Bause J, Scheffler K, Henning A (2020) Bent folded-end dipole head array for ultra-high-field MRI turns "dielectric resonance" from an enemy to a friend. Magn Reson Med. https://doi.org/10.1002/mrm.28336

33. Avdievich NI, Solomakha G, Ruhm L, Scheffler K, Henning A (2020) Decoupling of folded-end dipole antenna elements of a 9.4 T human head array using an RF shield. NMR Biomed. https://doi.org/10.1002/nbm.4351:e4351

34. Oezerdem C, Winter L, Graessl A, Paul K, Els A, Weinberger O, Rieger J, Kuehne A, Dieringer M, Hezel F, Voit D, Frahm J, Niendorf T (2016) 16-channel bow tie antenna transceiver array for cardiac MR at 7.0 tesla. Magn Reson Med 75(6):2553–2565

35. Paska J, Cloos MA, Wiggins GC (2018) A rigid, stand-off hybrid dipole, and birdcage coil array for 7 T body imaging. Magn Reson Med 80(2):822–832

36. Elabyad IA, Terekhov M, Stefanescu MR, Lohr D, Fischer M, Schreiber LM (2019) Design and evaluation of a novel symmetric multichannel transmit/receive coil array for cardiac MRI in Pigs at 7 T. IEEE Trans Microw Theory Tech 67(9):3928–3945

37. Elabyad IA, Terekhov M, Stefanescu MR, Lohr D, Fischer M, Schreiber LM (2019) Design of a novel antisymmetric coil array for parallel transmit cardiac MRI in pigs at 7 T. J Magn Reson 305:195–208

38. Elabyad IA, Terekhov M, Lohr D, Stefanescu MR, Baltes S, Schreiber LM (2020) A Novel mono-surface antisymmetric 8Tx/16Rx coil array for parallel transmit cardiac MRI in Pigs at 7T. Sci Rep 10(1):3117

39. Elabyad IA, Terekhov M, Bille M, Schreiber LM (2021) Design and implementation of Two 16-element antisymmetric transceiver coil arrays for parallel transmission human cardiac MRI at 7 T. IEEE Trans Microw Theory Tech 69(7):3540–3557

40. Elabyad IA, Terekhov M, Lohr D, Bille M, Hock M, Schreiber LM (2022) A novel antisymmetric 16-element transceiver dipole antenna array for parallel transmit cardiac MRI in pigs at 7 T. NMR Biomed. https://doi.org/10.1002/nbm.4726:e4726

41. Lohr D, Terekhov M, Veit F, Schreiber LM (2020) Longitudinal assessment of tissue properties and cardiac diffusion metrics of the ex vivo porcine heart at 7 T: Impact of continuous tissue fixation using formalin. NMR Biomed 33(7):e4298

42. Lohr D, Terekhov M, Weng AM, Schroeder A, Walles H, Schreiber LM (2019) Spin echo based cardiac diffusion imaging at 7T: An ex vivo study of the porcine heart at 7T and 3T. PLoS ONE 14(3):e0213994

43. Lohr D, Thiele A, Stahnke M, Braun V, Smeir E, Spranger J, Brachs S, Klopfleisch R, Foryst-Ludwig A, Schreiber LM, Kintscher U, Beyhoff N (2022) Assessment of myocardial microstructure in a murine model of obesity-related cardiac dysfunction by diffusion tensor magnetic resonance Imaging at 7T. Front Cardiovasc Med 9:839714

44. Kozlov M, Turner R (2009) Fast MRI coil analysis based on 3-D electromagnetic and RF circuit co-simulation. J Magn Reson 200(1):147–152

45. Elabyad IA, Terekhov M, Hock M, Lohr D, Schreiber LM (2021) Development of a Dedicated Mono-surface 16-Element Transceiver Dipole Antenna Array for Parallel Transmission Cardiac MRI in Pigs at 7 Tesla. Proc Intl Soc Mag Reson Med 1577.

46. Metzger GJ, Snyder C, Akgun C, Vaughan T, Ugurbil K, Van de Moortele PF (2008) Local B-1(+) shimming for prostate imaging with transceiver arrays at 7T based on subject-dependent transmit phase measurements. Magn Reson Med 59(2):396–409

47. Chung S, Kim D, Breton E, Axel L (2010) Rapid B1+ mapping using a preconditioning RF pulse with TurboFLASH readout. Magn Reson Med 64(2):439–446

48. Skare S, Hedehus M, Moseley ME, Li TQ (2000) Condition number as a measure of noise performance of diffusion tensor data acquisition schemes with MRI. J Magn Reson 147(2):340–352

49. F-C Y. http://dsi-studio.labsolver.org. Accessed April 22 2016

50. Kotu LP, Engan K, Skretting K, Maloy F, Orn S, Woie L, Eftestol T (2013) Probability mapping of scarred myocardium using texture and intensity features in CMR images. Biomed Eng Online 12:91

51. Magat J, Ozenne V, Cedilnik N, Naulin J, Haliot K, Sermesant M, Gilbert SH, Trew M, Haissaguerre M, Quesson B, Bernus O (2021) 3D MRI of explanted sheep hearts with submillimeter isotropic spatial resolution: comparison between diffusion tensor and structure tensor imaging. MAGMA 34(5):741–755

52. Schuster A, Zarinabad N, Ishida M, Sinclair M, van den Wijngaard JP, Morton G, Hautvast GL, Bigalke B, van Horssen P, Smith N, Spaan JA, Siebes M, Chiribiri A, Nagel E (2014) Quantitative assessment of magnetic resonance derived myocardial perfusion measurements using advanced techniques: microsphere validation in an explanted pig heart system. J Cardiovasc Magn Reson 16:82

53. Chiribiri A, Schuster A, Ishida M, Hautvast G, Zarinabad N, Morton G, Otton J, Plein S, Breeuwer M, Batchelor P, Schaeffter T, Nagel E (2013) Perfusion phantom: an efficient and reproducible method to simulate myocardial first-pass perfusion measurements with cardiovascular magnetic resonance. Magn Reson Med 69(3):698–707

54. Terekhov M, Elabyad IA, Schreiber LM (2021) Global optimization of default phases for parallel transmit coils for ultra-high-field cardiac MRI. PLoS ONE 16(8):e0255341